Multimode communication through the turbulent atmosphere

LILIANA BORCEA[1,2], JOSSELIN GARNIER[3,4], AND KNUT SØLNA[5,6]

[1] Department of Mathematics, University of Michigan, Ann Arbor, MI 48109
[3] CMAP, CNRS, Ecole polytechnique, Institut Polytechnique de Paris, 91128 Palaiseau Cedex, France
[5] Department of Mathematics, University of California at Irvine, Irvine, CA 92697
[2] borcea@umich.edu
[4] josselin.garnier@polytechnique.edu
[6] ksolna@math.uci.edu

Compiled June 13, 2020

A central question in free-space optical communications is how to improve the transfer of information between a transmitter and receiver. The capacity of the communication channel can be increased by multiplexing of independent modes using either: (1) the MIMO (Multiple-Input-Multiple-Output) approach, where the communication is done with modes obtained from the singular value decomposition of the transfer matrix from the transmitter array to the receiver array, or (2) the OAM (Orbital Angular Momentum) approach, which uses vortex beams that carry angular momenta. In both cases, the number of usable modes is limited by the finite aperture of the transmitter and receiver, and the effect of the turbulent atmosphere. The goal of this paper is twofold: First, we show that the MIMO and OAM multiplexing schemes are closely related. Specifically, in the case of circular apertures, the leading singular vectors of the transfer matrix which are useful for communication are essentially the same as the commonly used Laguerre-Gauss vortex beams, provided these have a special radius that depends on the wavelength, the distance from the transmitter to the receiver and the ratio of the radii of their apertures. Second, we characterize the effect of atmospheric turbulence on the communication modes using the phase screen method put in the mathematical framework of beam propagation in random media.

http://dx.doi.org/10.1364/ao.XX.XXXXXX

1. INTRODUCTION

In free-space optical communications, one seeks to transfer information between a transmitter array and a receiver array using laser beams. It is an important technology for line-of-sight communication between moving locations (e.g. in satellite communications), or for settings where fiber-based systems do not exist. A central question is how to increase the capacity of the communication channel via multiplexing independent sub-channels called modes. Typically, these are defined as special orthogonal solutions of the Helmholtz equation in homogeneous transmission media. Orbital Angular Momentum (OAM) beams [1, 2] are such solutions, also known as vortex beams [Chapter 2, 3], because they exhibit a vortex on the axis of the beam, where the intensity is zero and the phase is not defined. Popular examples of OAM beams are: (1) Bessel beams, which have the desirable non-diffractive property, but cannot be realized because they carry infinite energy [4]. In practice, these are approximated via some truncation strategy to obtain, for example, the Bessel-Gauss beams [5]. (2) Hermite-Gauss and Laguerre-Gauss beams [Section 16, 6], which are solutions of the paraxial approximation of the Helmholtz equation in rectangular and cylindrical coordinates, respectively. The Laguerre-Gauss beams are of special interest because they are easily realizable in practice [7, 8].

OAM beams have received much attention because by changing their azimuthal angle θ dependency $\exp(ij\theta)$, where the integer j is the so-called topological charge, one can create in theory an infinite number of modes. However, only finitely many modes will have significant power within the finite apertures of the transmitter and receiver. Moreover, the interaction of the beams with the atmosphere and noise are limiting factors that cause loss of orthogonality of the modes at the receiver end. This causes channel cross-talk and loss of information [7, 9].

The finite aperture size can be taken into account by using a Multiple-Input-Multiple-Output (MIMO) multiplexing approach based on the Singular Value Decomposition of the transfer matrix [10] from the transmitter array to the receiver array. The SVD gives the optimal communication modes, which are the singular vectors corresponding to the significant (i.e., distinguishable from noise) singular values . The transmission modes are the right singular vectors and the receiver modes are

the left singular vectors.

The ideal SVD-based MIMO multiplexing is carried out for the measured transfer matrix, which takes into account atmospheric turbulence effects, no matter how strong they are. However, it may not be feasible in some applications, especially since temporal changes of the atmosphere require repeated measurements. The alternative is to use the SVD of a model transfer matrix calculated in a reference homogeneous medium, and communicate through weakly turbulent media, so that the modes calculated with the homogeneous model are still appropriate. Studies like [7, 9, 11] test the limits of this approach by quantifying experimentally, or with numerical simulations, how the modes are affected by the atmosphere.

A much debated issue has been the advantage of using OAM beams versus MIMO multiplexing [12–14]. Here we show that in fact the two approaches are closely related. We consider a paraxial beam propagation model and a continuum aperture approximation, under which we can approximate the transmission and receiver arrays by continuous disk-shaped apertures. The continuum aperture approximation is accurate for closely spaced sensors in the transmitter and receiver arrays, separated by less than the Rayleigh resolution limit, which is typically the case. It makes it possible to describe the modes as singular functions of a linear integral operator. The advantage is that these singular functions have explicit expressions that can be compared easily with the vortex beams. We consider disk-shaped apertures because they are commonly used in practice [7, 8]. Our analysis extends to any shape of the apertures, although the modes will not have explicit expressions unless these shapes are simple such as squares, rectangles or disks.

The SVD of the model transfer matrix for disk-shaped transmitter and receiver apertures with radii a_T and a_R has an explicit solution in terms of the circular prolate spheroidal functions [15, 16]. If we denote by λ the wavelength and by L the transmission distance, then the matrix has

$$N = \frac{\pi a_R^2}{[\lambda L/(2a_T)]^2} \tag{1}$$

singular values that are very close to one, and the remaining ones plunge rapidly toward zero. A large singular value means that the mode carries large power within the receiver aperture and is thus less affected by noise. Physically, the number N can be interpreted as the number of focal spots of linear size $\lambda L/(2a_T)$ that fit in the receiver aperture area πa_R^2. The interesting regime for communications corresponds to a large N, so that one can multiplex the many N useable modes.

It has been observed in [17, 18] that in the case of soft disk-shaped apertures, with Gaussian apodization, the convenient Laguerre-Gauss beams are the modes given by the SVD. The similarity of some Laguerre-Gauss beam modes and the circular prolate spheroidal functions was also noticed in [10, 18]. Using the theory of circular prolate spheroidal functions [15], we show that in fact the Laguerre-Gauss beam modes are the significant modes given by the SVD even for hard aperture thresholding, as long as their radius is carefully calibrated in terms of the wavelength λ, the propagation distance L, and the ratio a_T/a_R, as prescribed by the forthcoming formula (16).

Some recent studies [9] have found that Bessel-Gauss OAM beams are more robust to turbulence effects than the Laguerre-Gauss beams. Here we show that, provided the Laguerre-Gauss beams are calibrated as stated above, the opposite is true. We study the effect of turbulence using the mathematical theory of paraxial wave propagation in random media with statistics corresponding to Kolmogorov type turbulence. We use the theory to put numerical phase screen simulation results [19, 20] in a mathematical framework and to clarify the link between the phase screen parameters and the turbulence model.

The paper is organized as follows. In Section 2 we consider laser beam propagation in homogeneous free space and study different candidates to multiplexing schemes. In particular, we identify the leading singular vectors of the transfer matrix that are used in the MIMO approach and show that they are related to Gauss-Laguerre modes. In Section 3 we consider laser beam propagation through the turbulent atmosphere and give the Itô-Schrödinger mathematical model which characterizes the statistics of the transmitted beams. In Section 4 we quantify the robustness of different multiplexing schemes with respect to the turbulent atmosphere. We conclude with a brief summary in section 5.

2. HOMOGENEOUS PARAXIAL WAVE EQUATION

In this section we describe classical beams that exhibit orthogonality when they propagate through a homogeneous medium. They are approximate solutions of the Helmholtz equation of the form $u(r,\theta,z)\exp(ikz)$, with $u(r,\theta,z)$ satisfying the paraxial wave equation [6],

$$2ik\partial_z u(r,\theta,z) + \Delta_\perp u(r,\theta,z) = 0, \tag{2}$$

where $k = 2\pi/\lambda$ is the wavenumber. Because we assume circular apertures of the transmitter and receiver arrays, we use the cylindrical coordinates (r,θ,z), with z measured along the axis of the beam, radius r and azimuth θ. The operator

$$\Delta_\perp = r^{-1}\partial_r\big(r\partial_r\,\cdot\,\big) + r^{-2}\partial_\theta^2$$

is the transverse Laplacian. We assume throughout an input beam profile $u(r,\theta,z=0)$ with slow variation on the scale of the wavelength λ, so that the paraxial approximation is valid.

2.1. Bessel-Gauss beams

Let $\beta > 0$ and $r_o > 0$ be such that $k \gg \beta$ and $kr_o \gg 1$. For any integer j, the input profile of the j-th Bessel-Gauss beam is [Section 12.1, 3]

$$u_j^{\mathrm{BG}}(r,\theta,z=0) = J_j(\beta r)\exp\Big(-\frac{r^2}{r_o^2}\Big)\exp\left(ij\theta\right), \tag{3}$$

where J_j is the Bessel function of the first kind. After propagating a distance z in the homogeneous medium, the output profile of the beam is

$$u_j^{\mathrm{BG}}(r,\theta,z) = \frac{r_o}{r_z}J_j\Big(\frac{\beta r}{1+i\frac{z}{z_{\mathrm{R}}}}\Big)\exp\left[\Big(r^2+\frac{\beta^2 z^2}{k^2}\Big)\Big(-\frac{1}{r_z^2}+i\frac{k}{2R_z}\Big)\right] \times \exp\left[ij\theta - i\frac{\beta^2}{2k}z - i\,\mathrm{atan}\Big(\frac{z}{z_{\mathrm{R}}}\Big)\right]. \tag{4}$$

Here $z_{\mathrm{R}} = kr_o^2/2$ is the Rayleigh length, r_z is the radius of the beam at distance z,

$$r_z = r_o\Big(1+\frac{z^2}{z_{\mathrm{R}}^2}\Big)^{\frac{1}{2}}, \tag{5}$$

and R_z is the radius of curvature of the wavefront,

$$R_z = z\Big(1+\frac{z_{\mathrm{R}}^2}{z^2}\Big). \tag{6}$$

If $r_o \to +\infty$ then Eq. (4) tends to

$$u_j(r,\theta,z) = J_j(\beta r)\exp\Big(ij\theta - i\frac{\beta^2}{2k}z\Big),$$

the ideal j-th Bessel beam [Section 12.1, 3] which is diffraction-free, but cannot be realized in practice as it has infinite energy (L^2-norm).

2.2. Laguerre-Gauss beams

Let $r_o > 0$ be such that $kr_o \gg 1$ and p, j be integers with $p \geq 0$. The input profile of the (p,j)-th Laguerre-Gauss mode is [Section 2.2, 3]

$$u^{\rm LG}_{p,j}(r,\theta,z=0) = \sqrt{\frac{2p!}{\pi(|j|+p)!}}\Big(\frac{\sqrt{2}r}{r_o}\Big)^{|j|}L_p^{|j|}\Big(\frac{2r^2}{r_o^2}\Big) \times \exp\Big(-\frac{r^2}{r_o^2} + ij\theta\Big), \quad (7)$$

where

$$L_p^j(s) = \frac{e^s s^{-j}}{p!}\frac{d^p}{ds^p}(e^{-s}s^{p+j})$$

is the generalized Laguerre polynomial. The input Laguerre-Gauss profiles are not compactly supported. However, they are approximately zero outside disks with radii of the order of r_o for the low-order modes, and of the order $\sqrt{|j|}r_o$ for high mode indices $|j|$ [21].

After propagation over a distance z in the homogeneous medium, the Laguerre-Gauss beam profiles widen due to diffraction,

$$u^{\rm LG}_{p,j}(r,\theta,z) = \sqrt{\frac{2p!}{\pi(|j|+p)!}}\frac{r_o}{r_z}\Big(\frac{\sqrt{2}r}{r_z}\Big)^{|j|}L_p^{|j|}\Big(\frac{2r^2}{r_z^2}\Big) \times \exp\Big[r^2\Big(-\frac{1}{r_z^2} + \frac{ik}{2R_z}\Big)\Big] \times \exp\Big[ij\theta - i(|j|+2p+1)\mathrm{atan}\Big(\frac{z}{z_{\rm R}}\Big)\Big], \quad (8)$$

where r_z is the beam radius defined in Eq. (5) and R_z is the radius of curvature of the wavefront defined in Eq. (6).

2.3. SVD-based MIMO multiplexing

Bessel-Gauss and Laguerre-Gauss beams are two of the many examples of orthogonal modes that carry an angular momentum i.e., a phase of the form $\exp(ij\theta)$ which is kept invariant during the propagation. In theory, for transmission through the homogeneous medium, and for infinite transmitter and receiver apertures, the countably infinite family of such orthogonal modes could be used to obtain an indefinite increase in the capacity of the communication channel. In reality, this cannot be achieved due to the finite transmitter and receiver apertures and heterogeneity in the transmission medium. We describe here the limitations imposed by the finite apertures and postpone until section 3 the discussion of the effect of a turbulent transmission medium.

The SVD of the model transfer[1] matrix $\boldsymbol{\mathcal{T}}$ gives a systematic approach for describing which beams are better suited for communication between the transmitter and receiver arrays, at distance L. Assuming that the transmitter array has n_T elements and the receiver array has n_R elements, $\boldsymbol{\mathcal{T}}$ is an $n_R \times n_T$ matrix with complex entries $\mathcal{T}_{t,r}$ defined by the wave at the $r-$th receiver, in the reference homogeneous medium, due to a unit input at the $t-$th transmitter. The model matrix $\boldsymbol{\mathcal{T}}$ can be computed by solving the wave equation in the homogeneous medium. Its right singular vectors are the orthonormal input profiles that can be used in multiplexing at the transmitter array. The left singular vectors form the orthonormal basis that can be used for demultiplexing at the receiver array.

As mentioned in the introduction, we present the SVD analysis for disk-shaped apertures, because they are often used in practice. Other apertures can be considered in principle, but the SVD will not be explicit unless they have simple shapes.

2.4. SVD in the continuum approximation

If the transmitters and receivers are closely spaced in the arrays with radii a_T and a_R, in the sense that their linear size is smaller than the Rayleigh resolution limit $\lambda L/[2\max\{a_T, a_R\}]$, we can approximate the arrays by the continuous apertures $\mathcal{A}_T$ and $\mathcal{A}_R$ defined by

$$\mathcal{A}_{T,R} = \{\boldsymbol{x} = (r\cos\theta, r\sin\theta),\ 0 \leq r \leq a_{T,R},\ \theta \in [0, 2\pi]\}.$$

In this continuous setting, the transfer matrix becomes the linear integral operator $\boldsymbol{\mathcal{T}} : L^2(\mathcal{A}_T) \mapsto L^2(\mathcal{A}_R)$,

$$u(\boldsymbol{x}, L) = \boldsymbol{\mathcal{T}}u_o(\boldsymbol{x}) = \int_{\mathcal{A}_T} u_o(\boldsymbol{x}')G\left((\boldsymbol{x}, L), (\boldsymbol{x}', 0)\right)d\boldsymbol{x}', \quad (9)$$

for $\boldsymbol{x} \in \mathcal{A}_R$. Here $u_o(\boldsymbol{x}) = u(\boldsymbol{x}, 0)$ is the input beam profile at the transmitter array and the kernel is the Green's function of the paraxial equation (2), given by

$$G\left((\boldsymbol{x}, L), (\boldsymbol{x}', 0)\right) = \frac{k}{2i\pi L}\exp\Big(i\frac{k|\boldsymbol{x}-\boldsymbol{x}'|^2}{2L}\Big). \quad (10)$$

The right singular functions of $\boldsymbol{\mathcal{T}}$, which define the transmission modes in the MIMO multiplexing, are of the form

$$u_o(\boldsymbol{x}) = \exp\Big(-i\frac{k|\boldsymbol{x}|^2}{2L}\Big)v\Big(\frac{\boldsymbol{x}}{a_T}\Big), \quad \boldsymbol{x} \in \mathcal{A}_T, \quad (11)$$

where $v(\boldsymbol{s})$ are the right singular functions of the linear integral operator $\mathcal{S} : L^2(B(\boldsymbol{0}, 1)) \mapsto L^2(B(\boldsymbol{0}, 1))$ defined by

$$\mathcal{S}v(\boldsymbol{s}) = \int_{B(\boldsymbol{0},1)} v(\boldsymbol{s}')\exp\left(-iC\boldsymbol{s}\cdot\boldsymbol{s}'\right)d\boldsymbol{s}', \qquad \boldsymbol{s} \in B(\boldsymbol{0}, 1). \quad (12)$$

Here $B(\boldsymbol{0}, 1)$ denotes the unit disk centered at the origin $\boldsymbol{0}$ of the cross-range plane, and

$$C = \frac{ka_Ta_R}{L}. \quad (13)$$

The operator $\mathcal{S}$ was studied by Slepian [15]. Its singular functions $v(\boldsymbol{s})$ are the generalized prolate spheroidal functions, its first $N = C^2/\pi$ singular values (recall Eq. (1)) are close to 1, and the remaining ones plunge rapidly to zero.

We are interested in the case $C \gg 1$, where there are $N \gg 1$ transmission modes of the form (11) available for multiplexing. For such C, it follows from [Eq. (67), 15] that the leading singular functions of $\mathcal{S}$ behave like scaled Gauss-Laguerre functions

$$v_{p,j}(\boldsymbol{s}) = \exp\Big(-\frac{C|\boldsymbol{s}|^2}{2}\Big)L_p^{|j|}(C|\boldsymbol{s}|^2)(\sqrt{C}|\boldsymbol{s}|)^{|j|}e^{ij\mathrm{arg}(\boldsymbol{s})}, \quad (14)$$

[1] We assume that it is not feasible to measure the transfer matrix, which depends on the turbulent atmosphere, but that it is possible to compute the model transfer matrix $\mathcal{T}$ in a homogeneous medium.

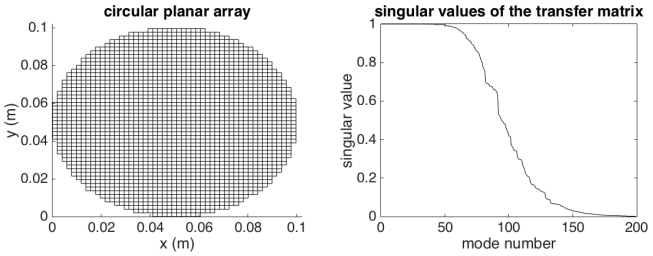

Fig. 1. Left: planar array with $n = 2063$ square elements with size 2mm in the disk-shaped aperture $\mathcal{A}$ of radius $a = 5$cm. Right: The first 200 singular values of the transfer matrix for transmission distance $L = 1$km and wavelength $\lambda = 850$nm.

for integers p, j, with $p \geq 0$. Thus, we conclude from Eq. (11) that, up to multiplicative constants, the transmission modes are vortex beams of the form (7),

$$u_{p,j}(\boldsymbol{x}, z = 0) = \exp\Big(-i\frac{k|\boldsymbol{x}|^2}{2L} - \frac{|\boldsymbol{x}|^2}{r_o^2}\Big) L_p^j\Big(\frac{2|\boldsymbol{x}|^2}{r_o^2}\Big) |\boldsymbol{x}|^j e^{ij\arg(\boldsymbol{x})}, \tag{15}$$

but for the special initial radius

$$r_o = \frac{\sqrt{2La_T}}{\sqrt{ka_R}}. \tag{16}$$

They correspond to the following leading singular values of $\mathcal{T}$ [Eq. (93), 15],

$$\mathfrak{S}_{p,j} = 1 - \frac{\pi 2^{2|j|+4p+3} C^{|j|+2p+1} e^{-2C}}{p!(p+|j|)!}\big[1 + O(C^{-1})\big]. \tag{17}$$

Note that the quadratic phase in the first factor in Eq. (15) makes the beam focus at distance (beam waist) $L/(1 + a_R^2/a_T^2)$. The beam then diffracts from there to the receiver array, to get an output profile that is similar to the transmitted one, but rescaled by the factor a_R/a_T.

2.5. Illustration

We consider throughout a practical setup for free-space optical communication with monochromatic laser beams [9]. The calculations are carried out as explained in appendix A. The wavelength is $\lambda = 850$nm, and the transmitter and receiver arrays are identical, with circular aperture $\mathcal{A}$ of radius $a = a_T = a_R = 5$cm. The arrays have $n = n_T = n_R = 2063$ square elements with side length 2mm (see left plot in Fig. 1). The transmission distance is $L = 1$km. Note that the aperture is not centered at the origin $(0, 0)$, but at $(5, 5)$cm. All the beam axes are shifted to pass through this center. The SVD analysis described in section 2.4 in the continuum setting is relevant here, because the Rayleigh resolution limit $\lambda_o L/(2a) = 8.5$mm is larger than the 2mm size of the elements of the arrays.

After computing the $n \times n$ transfer matrix in the homogeneous medium and carrying out its SVD, we find the singular values displayed in the right plot in Fig. 1. There are approximately 100 large ones, which is close to the theoretical estimate (1) of the essential rank of the integral operator (9) that predicts $N = 109$. As explained in more detail in appendix A, the right singular vectors give the orthonormal input profiles to be used in the MIMO multiplexing. The left singular vectors give the basis on which we project the wave at the receiver array, for demultiplexing. In our illustration the transmitter and receiver arrays are identical, so the transfer matrix is complex symmetric

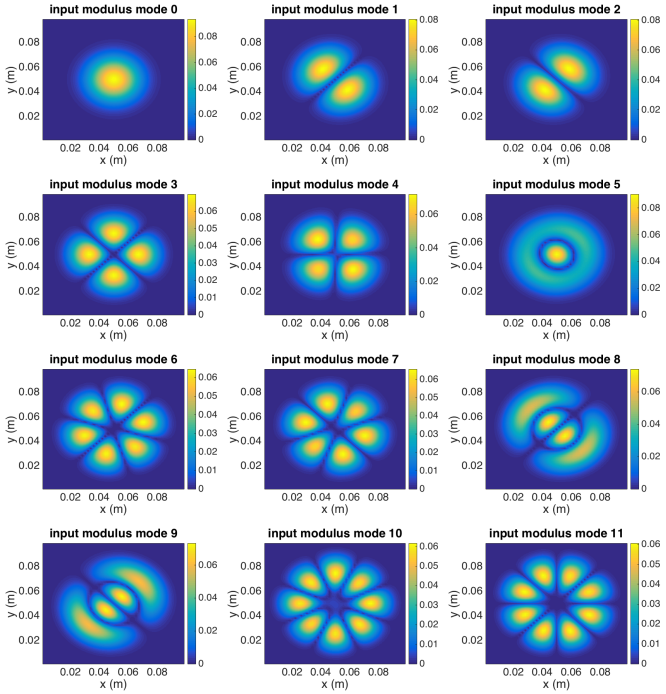

Fig. 2. Moduli of the mode profiles. The axes are in meters.

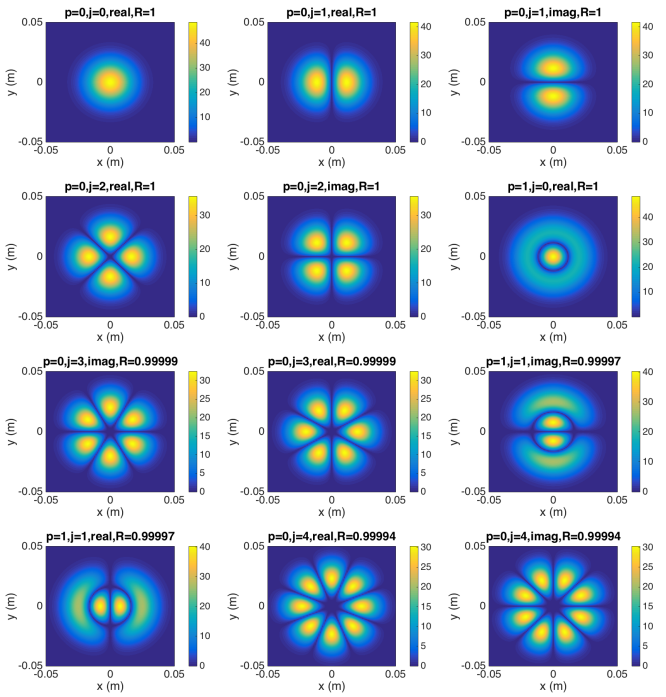

Fig. 3. Absolute values of the real and imaginary parts of the Laguerre-Gauss modes with radius $r_o = 1.64$cm. The profiles are sorted according to the power fraction R in the transmitter aperture. The axes are in meters.

and the right and left singular vectors are the same. We ensure that this is the case in the computations by using the symmetric (Takagi) SVD.

The mode profiles are stepwise constant functions on the elements of the array, with values given by the singular vectors. We plot in Fig. 2 the moduli of the first 12 modes. For compar-

ison, we also display in Fig. 3 the absolute values of the real and imaginary parts of the Laguerre-Gauss modes with initial radius $r_o = 1.64$cm calculated from Eq. (16). These modes are sorted according to their power fraction in $\mathcal{A}$. As expected from Eq. (15), the plots in Figs. 2 and 3 are basically the same, aside from a rotation by the angle $\pi/4$, which is irrelevant because $\mathcal{A}$ is rotation invariant.

The estimates of the eigenvalues can be see in Table 1, where we display the factors

$$\mathfrak{S}'_{p,j} = \frac{\pi 2^{2|j|+4p+3} C^{|j|+2p+1} e^{-2C}}{p!(p+|j|)!}.$$

in the right hand side of Eq. (17). The sorting in the table is the same as that based on the power fraction in $\mathcal{A}$, used in Fig. 3.

(p,j)	$(0,0)$	$(0,1)$	$(0,2)$	$(1,0)$	$(0,3)$	$(1,1)$	$(0,4)$
$\mathfrak{S}'_{p,j}$	$4\cdot 10^{-14}$	$3\cdot 10^{-12}$	10^{-10}	$2\cdot 10^{-10}$	$3\cdot 10^{-9}$	$8\cdot 10^{-9}$	$5\cdot 10^{-8}$

Table 1. Values of $\mathfrak{S}'_{p,j}$ sorted in increasing order.

2.6. Discussion

The results in section 2.3 reconcile the MIMO approach, where the singular vectors of the transfer matrix are used for multiplexing, and the OAM approach, in which Laguerre-Gauss beams are used as transmission modes [section 6.2 3]. The useful modes given by the SVD correspond to the N large singular values. We showed that they are the same as the Laguerre-Gauss vortex beams defined in Eq. (7), provided that their initial radius r_o is chosen as in Eq. (16). In the illustrations in Figs. 2 and 3 we chose $a_r = a_T$, so that the beam is affected by diffraction at the transmission distance $L = z_R = kr_o^2/2$. For different radii of the transmitter and receiver, the Rayleigh length satisfies $z_R = La_T/a_R$, so the larger the transmitter aperture, the smaller the diffraction effect.

At large mode numbers, corresponding to small singular values and thus negligible power within the receiver aperture, the Laguerre-Gauss modes and the SVD modes differ, because the latter are compactly supported in the aperture and the former extend outside the aperture. Obviously, such modes are not useful for transmitting information.

3. COMMUNICATION THROUGH TURBULENCE

The results in section 2 show that in the ideal case of transmission through a homogeneous medium, the leading N modes determined from the SVD decomposition of the transfer matrix should be used as transmission modes. Moreover, in the case of dense planar circular arrays and $N \gg 1$, these modes are the Laguerre-Gauss vortex beams with initial radius defined in Eq. (16). We now seek to quantify how such a multiplexing scheme degrades in a turbulent transmission medium.

We consider only weak turbulence, meaning that the transmission distance L and the turbulence parameters that determine the turbulence power spectral density (turbulence strength C_n and outer scale of turbulence L_0, see Eq. (24)) are such that the main effects of turbulence on wave propagation are moderate wavefront aberrations. In other words, the coherent part of the received beam (i.e., its statistical expectation) is larger than or of the same order as the turbulence induced random fluctuations. If the turbulence is stronger, then the modes of the model transmission matrix calculated in the reference homogeneous medium are not useful anymore. Instead, the multiplexing should be based on the SVD of the measured transfer matrix.

It was shown in [9] via numerical simulations, which do not account for finite transmitter and receiver apertures, that Bessel-Gauss beams outperform Laguerre-Gauss beams in channel efficiency through a turbulent medium. The earlier paper [19] studied the probability of detection of the angular momentum when a Laguerre-Gauss mode is transmitted through a turbulent medium, by using a formal propagation model. A similar approach was used in [20], where the role of the turbulence strength measured in terms of the Fried parameter (relative to the aperture) was discussed. Further insight using this framework was provided in [11], where diffractive effects for relatively small aperture were discussed both from analytic and experimental viewpoints.

Here we present a framework where the role of the turbulence is taken into account in a rigorous fashion, and connect it to the phase screen model for numerical wave propagation. We also derive explicit formulas for the cross-correlations of the wave field in a specific scaling regime, corresponding to weak diffraction. These formulas give good predictions of the performance of MIMO and OAM multiplexing schemes, even for moderate diffraction, as explained in section 4.

3.1. Random paraxial wave equation and phase screen

Beam propagation through a turbulent medium can be described mathematically by the random paraxial wave equation

$$2ik\partial_z u(\boldsymbol{x},z) + \Delta_\perp u(\boldsymbol{x},z) + k^2 V(\boldsymbol{x},z) u(\boldsymbol{x},z) = 0, \tag{18}$$

for $\boldsymbol{x} \in \mathbb{R}^2$ and $z > 0$, with initial condition

$$u(\boldsymbol{x},0) = u_o(\boldsymbol{x}), \tag{19}$$

where $V(\boldsymbol{x},z)$ is a random potential. The phase screen method approximates the solution of this equation using a split-step Fourier method with grid step ℓ_z. This amounts to assuming that the random potential is stepwise constant in z over intervals with length ℓ_z,

$$V(\boldsymbol{x},z) = \sum_{n\geq 0} \mathbf{1}_{[n\ell_z,(n+1)\ell_z)}(z) V_n(\boldsymbol{x}). \tag{20}$$

Here $\mathbf{1}_I(z) = 1$ if $z \in I$ and 0 otherwise, and $V_n(\boldsymbol{x})$ are i.i.d. copies of a stationary two-dimensional Gaussian, zero-mean random field with covariance function

$$\mathbb{E}[V_n(\boldsymbol{x}) V_n(\boldsymbol{x}')] = \mathcal{R}(\boldsymbol{x}-\boldsymbol{x}'). \tag{21}$$

We assume isotropic statistics, with covariance given by the Matérn model $\mathcal{R}(\boldsymbol{x}) = \mathcal{R}_\nu(|\boldsymbol{x}|)$,

$$\mathcal{R}_\nu(r) = \frac{\sigma^2}{\Gamma(\nu)2^{\nu-1}} \left(\frac{2\sqrt{\nu}r}{\ell_c}\right)^\nu K_\nu\left(\frac{2\sqrt{\nu}r}{\ell_c}\right), \tag{22}$$

where K_ν is the modified Bessel function of second kind. The power spectral density is

$$\widehat{\mathcal{R}}(\boldsymbol{\kappa}) = \int_{\mathbb{R}^2} \mathcal{R}(\boldsymbol{x}) e^{-i\boldsymbol{\kappa}\cdot\boldsymbol{x}} d\boldsymbol{x} = \sigma^2 \frac{2^{2\nu+2}\pi\nu^{\nu+1}}{\ell_c^{2\nu}} \left(\frac{4\nu}{\ell_c^2} + |\boldsymbol{\kappa}|^2\right)^{-\nu-1} \tag{23}$$

and it depends on three hyperparameters: σ^2, ℓ_c and ν. The hyperparameter $\nu \in [1/2, \infty)$ characterizes the smoothness of the process (the realizations are ν'-Hölder continuous, for any $\nu' < \nu$), $\sigma^2 = \mathcal{R}(\mathbf{0})$ is the variance and ℓ_c is the correlation radius.

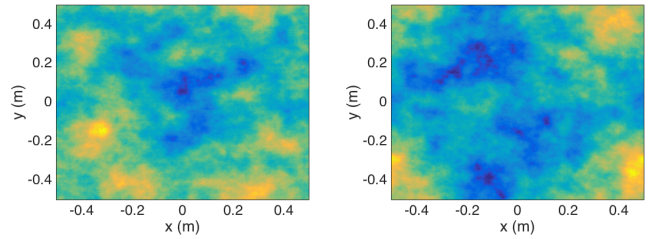

Fig. 4. Two independent phase screens, with $\ell_c = 20$ cm (outer scale $L_0 = 37$ cm). The coordinates x and y in the cross-range plane are in meters.

In the limit $\nu \to \infty$, we obtain from Eq. (22) the smooth Gaussian covariance model $\mathcal{R}(\boldsymbol{x}) = \sigma^2 \exp\big(-|\boldsymbol{x}|^2/\ell_c^2\big)$, whereas the other extreme $\nu = 1/2$ gives the rough exponential covariance model $\mathcal{R}(\boldsymbol{x}) = \sigma^2 \exp\big(-\sqrt{2}|\boldsymbol{x}|/\ell_c\big)$.

We consider henceforth $\nu = 5/6$, so that Eq. (22) gives a Kolmogorov-type model with outer scale proportional to ℓ_c and inner scale equal to zero. More explicitly, we recover from Eq. (23) the standard Kolmogorov model

$$\widehat{\mathcal{R}}(\boldsymbol{\kappa}) = 0.033 C_n^2 \left(\frac{1}{L_0^2} + |\boldsymbol{\kappa}|^2\right)^{-11/6}, \tag{24}$$

if we set $\nu = 5/6$, $\ell_c = 2\sqrt{\nu} L_0$, and $\sigma^2 = 0.033 C_n^2 L_0^{2\nu}/(4\pi\nu)$. With this parameterization, L_0 is the outer scale of turbulence and C_n^2 is the turbulence strength. In Fig. 4 we plot two realizations of a phase screen obtained with this model.

3.2. Itô-Schrödinger model

It is proved in [22] that in the high frequency and long range regime $\lambda_o \ll \ell_c, r_o \ll L$, the statistical distribution of the solution of (18–19) can be approximated by that of the solution of the Itô-Schrödinger equation

$$du(\boldsymbol{x},z) = \frac{i}{2k}\Delta_\perp u(\boldsymbol{x},z)\, dz + \frac{ik}{2} u(\boldsymbol{x},z) \circ dB(\boldsymbol{x},z), \tag{25}$$

with initial condition (19). This equation is written in Stratonovich form, and $B(\boldsymbol{x},z)$ is a Brownian field with covariance function

$$\mathbb{E}\big[B(\boldsymbol{x},z)B(\boldsymbol{x}',z')\big] = \ell_z \mathcal{R}(\boldsymbol{x}-\boldsymbol{x}') \min\{z,z'\}. \tag{26}$$

The statistical moments of the beam can be calculated using Itô's formula [23]. The first moment models the coherent (mean) wave and satisfies the damped Schrödinger equation

$$\partial_z \mathbb{E}[u(\boldsymbol{x},z)] = \frac{i}{2k}\Delta_\perp \mathbb{E}[u(\boldsymbol{x},z)] - \frac{k^2\sigma^2\ell_z}{8}\mathbb{E}[u(\boldsymbol{x},z)], \tag{27}$$

which can be solved explicitly to obtain

$$\mathbb{E}[u(\boldsymbol{x},z)] = \exp\left(-\frac{k^2\sigma^2\ell_z z}{8}\right) \int_{\mathbb{R}^2} u_o(\boldsymbol{x}') G\left((\boldsymbol{x},z),(\boldsymbol{x}',0)\right) d\boldsymbol{x}'. \tag{28}$$

The second factor (the integral) is the beam in the homogeneous medium propagated using the paraxial Green's function (10). The exponential decay models the loss of coherence of the beam due to scattering in the random medium.

The second moments of the beam can be described using the mean Wigner transform

$$\mathcal{W}(\boldsymbol{x},\boldsymbol{\kappa},z) = \int_{\mathbb{R}^2} \exp\big(-i\boldsymbol{\kappa}\cdot\boldsymbol{y}\big)\mathbb{E}\Big[u\Big(\boldsymbol{x}+\frac{\boldsymbol{y}}{2},z\Big)\overline{u}\Big(\boldsymbol{x}-\frac{\boldsymbol{y}}{2},z\Big)\Big] d\boldsymbol{y}, \tag{29}$$

where the bar denotes complex conjugate. This satisfies the radiative transport equation [22]

$$\partial_z \mathcal{W}(\boldsymbol{x},\boldsymbol{\kappa},z) + \frac{\boldsymbol{\kappa}}{k}\cdot\nabla_{\boldsymbol{x}}\mathcal{W}(\boldsymbol{x},\boldsymbol{\kappa},z) = \frac{k^2\ell_z}{4(2\pi)^2}\int_{\mathbb{R}^2}\widehat{\mathcal{R}}(\boldsymbol{\kappa}-\boldsymbol{\kappa}') \times\Big[\mathcal{W}(\boldsymbol{x},\boldsymbol{\kappa}',z) - \mathcal{W}(\boldsymbol{x},\boldsymbol{\kappa},z)\Big] d\boldsymbol{\kappa}', \tag{30}$$

which can be solved explicitly

$$\mathcal{W}(\boldsymbol{x},\boldsymbol{\kappa},z) = \frac{1}{(2\pi)^2}\iint_{\mathbb{R}^2\times\mathbb{R}^2}\widehat{\mathcal{W}}_o(\boldsymbol{\zeta},\boldsymbol{y})\exp\Big[i\boldsymbol{\zeta}\cdot\Big(\boldsymbol{x}-\boldsymbol{\kappa}\frac{z}{k}\Big)\Big] \times\exp\left[-i\boldsymbol{\kappa}\cdot\boldsymbol{y} + \frac{k^2\ell_z}{4}\int_0^z \mathcal{R}\Big(\boldsymbol{y}+\boldsymbol{\zeta}\frac{z'}{k}\Big) - \mathcal{R}(\boldsymbol{0})dz'\right] d\boldsymbol{\zeta}d\boldsymbol{y}, \tag{31}$$

for $\widehat{\mathcal{W}}_o$ defined in terms of the initial beam profile (19) by

$$\widehat{\mathcal{W}}_o(\boldsymbol{\zeta},\boldsymbol{y}) = \int_{\mathbb{R}^2}\exp(-i\boldsymbol{\zeta}\cdot\boldsymbol{x})u_o\Big(\boldsymbol{x}+\frac{\boldsymbol{y}}{2}\Big)\overline{u_o}\Big(\boldsymbol{x}-\frac{\boldsymbol{y}}{2}\Big)d\boldsymbol{x}. \tag{32}$$

3.3. Weakly diffraction regime

If the initial radius r_o of the beam and the correlation radius ℓ_c satisfy the scaling relations $kr_o^2 \gg z$ and $k\ell_c^2 \gg z$, we have a weak diffraction regime, where the expressions of the first and second moments of the beam simplify to

$$\mathbb{E}[u(\boldsymbol{x},z)] = u_o(\boldsymbol{x})\exp\Big(-\frac{k^2\sigma^2\ell_z z}{8}\Big), \tag{33}$$

and

$$\mathbb{E}\Big[u\Big(\boldsymbol{x}+\frac{\boldsymbol{y}}{2},z\Big)\overline{u}\Big(\boldsymbol{x}-\frac{\boldsymbol{y}}{2},z\Big)\Big] = u_o\Big(\boldsymbol{x}+\frac{\boldsymbol{y}}{2}\Big)\overline{u_o}\Big(\boldsymbol{x}-\frac{\boldsymbol{y}}{2}\Big) \times\exp\left[\frac{k^2\ell_z z}{4}\big(\mathcal{R}(\boldsymbol{y})-\mathcal{R}(\boldsymbol{0})\big)\right]. \tag{34}$$

This corresponds to multiplying the initial beam profile $u_o(\boldsymbol{x})$ with a global phase screen.

4. DEMULTIPLEXING AND CHANNEL EFFICIENCY

We now use the results in section 3 to quantify the recovery of a single input mode transmitted through a turbulent random medium. The recovery (demultiplexing) is studied by projecting the received wave field onto the output modes and looking at the detected powers. We compare the efficiencies of the different orthogonal beam families discussed in Section 2. We use throughout the setup described in section 2.5, where the apertures of the transmitter and receiver arrays are the same disk $\mathcal{A}$ of radius a.

4.1. SVD-based multiplexing

For the SVD-based MIMO scheme, suppose that the transmitter array transmits the j-th homogeneous input mode (right singular vector) $u(\boldsymbol{x},0) = u_j^{\mathrm{IN}}(\boldsymbol{x})$ for $j \geq 0$, and the receiver array projects the beam $u(\boldsymbol{x},L)$ transmitted through the turbulent medium at $z = L$ onto the homogeneous output modes (left singular vectors) $u_l^{\mathrm{OUT}}(\boldsymbol{x})$, for $l \geq 0$. The projection coefficients are defined by

$$p_{l,j} = \frac{\big|\int_{\mathcal{A}} u(\boldsymbol{x},L)\overline{u_l^{\mathrm{OUT}}}(\boldsymbol{x})d\boldsymbol{x}\big|^2}{\int_{\mathcal{A}}|u(\boldsymbol{x},L)|^2 d\boldsymbol{x}}. \tag{35}$$

Since $(u_l^{\mathrm{OUT}})_{l\geq 0}$ is a complete orthonormal basis of $L^2(\mathcal{A})$, the sum of these non-negative coefficients is $\sum_{l=0}^{\infty} p_{l,j} = 1$. The mode $u_j^{\mathrm{IN}}(\boldsymbol{x})$ is well transmitted when $p_{j,j}$ is close to one, so we can call the coefficient $p_{j,j}$ the channel efficiency.

In section 4.3 we calculate the coefficients (35) using the phase screen method described in section 3.1. We also compare them with the theoretical predictions of the Itô-Schrödinger model in the weakly diffractive regime, obtained by taking the expectation in Eq. (35) and using the simple second moment formula (34),

$$\mathcal{P}_{l,j} = \iint_{\mathcal{A}^2} u_j^{\mathrm{OUT}}(\boldsymbol{x})\overline{u_j^{\mathrm{OUT}}}(\boldsymbol{x}') \times \overline{u_l^{\mathrm{OUT}}}(\boldsymbol{x}) u_l^{\mathrm{OUT}}(\boldsymbol{x}')\mathcal{K}(\boldsymbol{x}-\boldsymbol{x}')d\boldsymbol{x}d\boldsymbol{x}', \tag{36}$$

where

$$\mathcal{K}(\boldsymbol{x}) = \exp\left[\frac{k^2\ell_z L}{4}\left(\mathcal{R}(\boldsymbol{x}) - \mathcal{R}(\boldsymbol{0})\right)\right]. \tag{37}$$

This formula predicts the channel efficiency

$$\mathcal{P}_{j,j} = \iint_{\mathcal{A}^2} |u_j^{\mathrm{OUT}}(\boldsymbol{x})|^2 |u_j^{\mathrm{OUT}}(\boldsymbol{x}')|^2 \mathcal{K}(\boldsymbol{x}-\boldsymbol{x}')d\boldsymbol{x}d\boldsymbol{x}'. \tag{38}$$

Note that since we assume identical transmitter and receiver apertures, the Rayleigh length calculated with the initial beam profile radius (16) equals the transmission distance L, so diffraction plays a role in the simulations. Nevertheless, the results in section 4.3 turn out to be in good agreement with the theoretical prediction estimates in Eqs. (36)–(38).

4.2. OAM multiplexing

Let us index the OAM modes by their topological charge $j \in \mathbb{Z}$ in the phase $\exp(ij\theta)$, which is natural for the Bessel-Gauss beams. The Laguerre-Gauss beams have a second index, but we already know from section 3 that the significant such modes (in terms of power in the aperture) are basically the same as the modes obtained with the SVD approach, discussed above. Therefore, here we focus attention on the Bessel-Gauss beams.

When the transmitter array emits the beam $u_j^{\mathrm{BG}}(\boldsymbol{x}, 0)$ defined in Eq. (3), the receiver array projects the transmitted beam $u(\boldsymbol{x}, L)$ at $z = L$ onto the theoretical profile $u_l^{\mathrm{BG}}(\boldsymbol{x}, L)$ given by Eq. (4). This corresponds to defining the projection coefficients

$$p_{l,j}^{\mathrm{BG}} := \frac{\left|\int_{\mathcal{A}} u(\boldsymbol{x}, L)\overline{u_l^{\mathrm{BG}}}(\boldsymbol{x}, L)d\boldsymbol{x}\right|^2}{\int_{\mathcal{A}} |u(\boldsymbol{x}, L)|^2 d\boldsymbol{x} \int_{\mathcal{A}} |u_l^{\mathrm{BG}}(\boldsymbol{x}, L)|^2 d\boldsymbol{x}}, \tag{39}$$

where j indexes the initial condition. Note that $\left(u_l^{\mathrm{BG}}(\boldsymbol{x}, L)\right)_{l\in\mathbb{Z}}$ is not a complete orthonormal basis of $L^2(\mathcal{A})$, so these coefficients do not sum to one, $\sum_{l=-\infty}^{\infty} p_{l,j}^{\mathrm{BG}} \neq 1$. We can, however, modify the definition of the coefficients to recover this normalization property, as in [19]. The new coefficients are

$$p_{l,j}^{\mathrm{OAM}} := \frac{\int_0^a \left|\int_0^{2\pi} u(r,\theta,L)e^{-il\theta}d\theta\right|^2 rdr}{2\pi \int_0^a \int_0^{2\pi} |u(r,\theta,L)|^2 d\theta r dr}, \tag{40}$$

and they satisfy $\sum_{l=-\infty}^{\infty} p_{l,j}^{\mathrm{OAM}} = 1$, by Parseval's equality.

In the weakly diffractive regime we have

$$u_{j,o}^{\mathrm{BG}}(\boldsymbol{x}) \equiv u_j^{\mathrm{BG}}(\boldsymbol{x}, 0) = u_j^{\mathrm{BG}}(\boldsymbol{x}, L),$$

and the theoretical predictions of the coefficients (39) and (40) given by the Itô-Schrödinger model are

$$\mathcal{P}_{l,j}^{\mathrm{BG}} = \frac{\iint_{\mathcal{A}^2} u_{j,o}^{\mathrm{BG}}(\boldsymbol{x})\overline{u_{j,o}^{\mathrm{BG}}}(\boldsymbol{x}')\overline{u_{l,o}^{\mathrm{BG}}}(\boldsymbol{x})u_{l,o}^{\mathrm{BG}}(\boldsymbol{x}')\mathcal{K}(\boldsymbol{x}-\boldsymbol{x}')d\boldsymbol{x}d\boldsymbol{x}'}{\left[\int_{\mathcal{A}} |u_{j,o}^{\mathrm{BG}}(\boldsymbol{x})|^2 d\boldsymbol{x}\right]\left[\int_{\mathcal{A}} |u_{l,o}^{\mathrm{BG}}(\boldsymbol{x})|^2 d\boldsymbol{x}\right]} \tag{41}$$

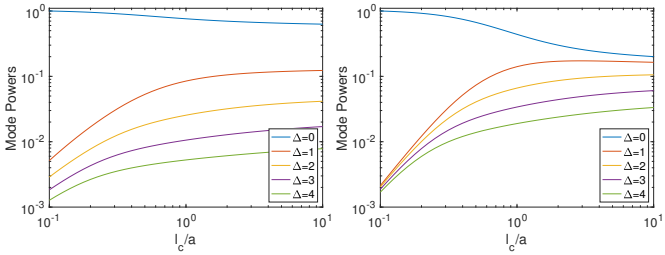

Fig. 5. Theoretical prediction Eq. (42) of the projection power for $j = 1$ (left plot) and $j = 9$ (right plot) as a function of ℓ_c/a. The curves are for the values of $\Delta = |l - j|$ shown in the legend.

and

$$\mathcal{P}_{l,j}^{\mathrm{OAM}} = \frac{\mathcal{N}_{l,j}^{\mathrm{OAM}}}{\mathcal{D}_{l,j}^{\mathrm{OAM}}}, \tag{42}$$

$$\mathcal{N}_{l,j}^{\mathrm{OAM}} = \int_0^a \iint_{[0,2\pi]^2} u_{j,o}^{\mathrm{BG}}(r,\theta)\overline{u_{j,o}^{\mathrm{BG}}}(r,\theta') \times \mathcal{K}_{\mathrm{OAM}}(r,\theta-\theta')e^{il(\theta'-\theta)}d\theta d\theta' r dr, \tag{43}$$

$$\mathcal{D}_{l,j}^{\mathrm{OAM}} = 2\pi \int_0^a \int_0^{2\pi} |u_{j,o}^{\mathrm{BG}}(r,\theta)|^2 d\theta r dr, \tag{44}$$

where $\mathcal{K}(\boldsymbol{x})$ is defined in Eq. (37) and

$$\mathcal{K}_{\mathrm{OAM}}(r,\theta) = \exp\left[\frac{k^2\ell_z L}{4}\left(\mathcal{R}_\nu\left(2r\left|\sin(\frac{\theta}{2})\right|\right) - \mathcal{R}_\nu(0)\right)\right]. \tag{45}$$

For illustration, we plot in Fig. 5 the coefficients $\mathcal{P}_{l,j}^{\mathrm{OAM}}$ as a function of ℓ_c/a for $j = 1$ (left plot) and $j = 9$ (right plot). We consider various values of $\Delta = |l - j|$ and note that the sign of $l - j$ does not affect $\mathcal{P}_{l,j}^{\mathrm{OAM}}$ in view of (3) and (43). We use $\sigma^2 k^2 \ell_z L = 8$, $r_o/a = 1$, $\beta a = 6$, $\nu = 5/6$, so that the mean field is strongly damped, but not completely vanished (see Eq. (33)). The results in Fig. 5 show that the cross talk between the modes becomes noticeable in a regime corresponding to $\ell_c \gtrsim a$. The numerical simulations in the next section are in this regime. Similar results were obtained in [19, 20] based on a phase screen model for the effect of the turbulence. Here we have put this model in the mathematical framework of beam propagation in random media, which makes explicit the scaling regime where it is valid, and we have clarified the link between the phase screen parameters and those of the model for the physical medium.

4.3. Numerical simulations

We now present numerical results obtained with the phase screen method described in section 3.1, for the setup in section 2.5, and the Kolmogorov-type model of the covariance obtained from definition (22). The hyperparameters in this model are $\nu = 5/6$, $\ell_c = 20$cm (i.e., $L_0 = 37$cm) and we consider three values of C_n^2 corresponding to a homogeneous medium ($C_n^2 = 0$), weak turbulence ($C_n^2 = 10^{-14}$) and stronger turbulence ($C_n^2 = 4 \cdot 10^{-14}$). The latter is near the limit of validity of multiplexing based on the model transfer matrix calculated in the reference homogeneous medium. As mentioned at the beginning of section 3, for stronger turbulence multiplexing should be based on the measured transfer matrix for the particular realization of the atmosphere through which the communication takes place. Our choices of parameters are similar to those in [9, 19], except for the outer scale L_0, which is smaller in our simulations. This does not have a big effect because the radius

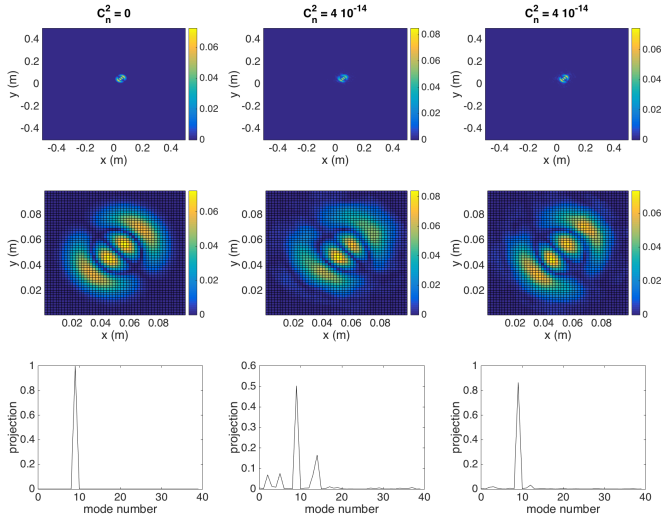

Fig. 6. The input beam is the $j = 9$-th mode obtained from SVD. The top two rows show the modulus of transmitted field. The second row is a zoom of the first i.e., the modulus of the field restricted to the receiver array. The axes are the coordinates in the cross-range plane, in meters. The bottom row plots the projection coefficients $p_{l,9}$ for $l = 0, \ldots, 39$. The left column is for the homogeneous transmission medium. The middle and right columns are for two realizations of the random medium with turbulence level $C_n^2 = 4 \cdot 10^{-14}$.

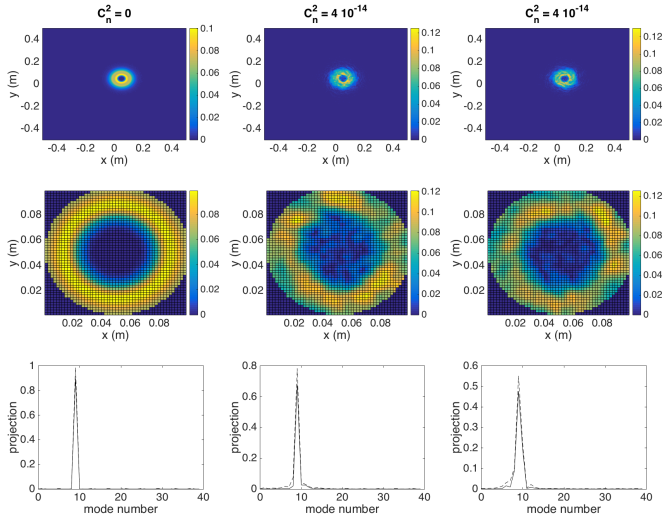

Fig. 7. The input beam is the $j = 9$-th input Bessel-Gauss mode with radius r_o given by (16). The top two rows show the modulus of transmitted field. The second row is a zoom of the first i.e., the modulus of the field restricted to the receiver array. The axes are the coordinates in the cross-range plane, in meters. The bottom row plots the projection coefficients $p_{l,9}^{\mathrm{BG}}$ (solid line) and $p_{l,9}^{\mathrm{OAM}}$ (dashed line) for $l = 0, \ldots, 39$. The left column is for the homogeneous transmission medium. The middle and right columns are for two realizations of the random medium with turbulence level $C_n^2 = 4 \cdot 10^{-14}$.

of the beams is smaller than the radius $a = 5$cm of the apertures, and therefore smaller than L_0. The wavelength is $\lambda = 850$nm and the transmission distance is $L = 1$km.

The SVD-based multiplexing is carried out using the SVD of the transfer matrix in the synthetic homogeneous medium. The transmitter and receiver aperture $\mathcal{A}$ is as in the left plot in Fig. 1, so in the simulations we shift the beam axes to pass through the center $(5, 5)$cm of $\mathcal{A}$.

In the top two rows of Fig. 6 we display the modulus of the beam at the receiver array, due to the initial profile given by the $j = 9$-th input SVD mode in Fig. 2. The results are obtained in two realizations of the turbulent random medium, for the stronger turbulence ($C_n^2 = 4 \cdot 10^{-14}$). We also display the projection coefficients Eq. (35). As expected, the channel efficiency is perfect ($p_{j,j} = 1$) in the homogeneous medium. It deteriorates in the turbulent medium, due to mode mixing, and the result is dependent on the realization of the medium.

Fig. 7 is the analogue of Fig. 6, except that the input beam is the $9-$th Bessel-Gauss mode. The main difference between Figs. 6 and 7 is that the power delivered by the Bessel-Gauss beam is mostly on the edges of the aperture, whereas for the SVD mode the power is well contained inside the aperture. This plays a role for higher mode numbers, because the Bessel-Gauss modes do not take the finite aperture into account and they deliver less and less power within the receiver array. See Fig. 8 for an illustration of this effect in the homogeneous medium.

The plots in Figs. 6 and 7 show that the channel efficiency varies from one realization of the random medium to another. Therefore, we display in Fig. 9 the mean channel efficiency obtained by averaging over 100 realizations of the random medium, and its standard deviation. The solid lines in these figures show the performance of Bessel-Gauss (black and blue lines) and SVD modes (red lines). We also plot with the dotted lines the theoretical predictions given by the Itô-Schrödinger model in the

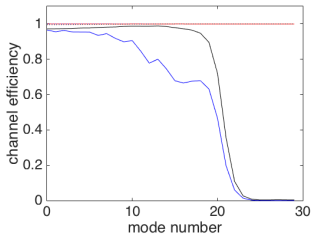

Fig. 8. Channel efficiencies in the homogeneous medium: $p_{j,j}^{\mathrm{BG}}$ (solid blue) and $p_{j,j}^{\mathrm{OAM}}$ (solid black) for the Bessel-Gauss modes and $p_{j,j}$ (solid red) for the SVD modes.

weakly diffractive regime. It appears that the low-order Bessel-Gauss modes are approximately as good as the low-order SVD modes. However, the mean channel efficiency of the Bessel-Gauss modes decreases much faster with the mode number. The channel efficiencies of the SVD modes also have smaller standard deviation.

The comparison between the red solid and dotted lines in the left plots of Fig. 9 shows a good quantitative agreement between formula (36) and the numerical simulations. This is because the profiles of the transmitted SVD modes are well captured by the receiver array and the predictions of the Itô-Schrödinger model in the weakly diffractive regime are reliable. When comparing the solid and dotted black and blue lines, we observe only qualitative agreements between formulas (41-42) and the numerical simulations. This is because the profiles of the transmitted Bessel-Gauss modes are poorly captured by the receiver array (the modes are concentrated on a thin annulus which diffracts).

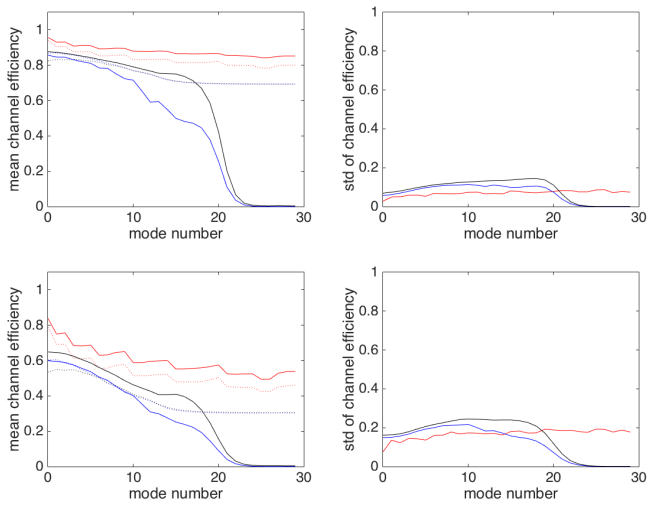

Fig. 9. Left: Mean channel efficiencies $p_{j,j}^{\mathrm{BG}}$ (solid blue) and $p_{j,j}^{\mathrm{OAM}}$ (solid black) for the Bessel-Gauss modes and $p_{j,j}$ for the homogeneous SVD modes (solid red). Right: Standard deviations of the channel efficiencies. Here $\sigma = 3\,10^{-9}$, $\ell_c = 20$ cm (i.e. $C_n^2 = 4\,10^{-14}$, $L_0 = 37$ cm), $a = 5$ cm, $\lambda_0 = 850$ nm, $L = 1000$ m. The dotted lines stand for the theoretical formulas (41) (dotted blue), (42) (dotted black), (36) (dotted red). Top row weak turbulence ($C_n^2 = 10^{-14}$) and bottom row stronger turbulence ($C_n^2 = 4 \cdot 10^{-14}$).

5. SUMMARY

We introduced a mathematical framework for studying MIMO and OAM multiplexing for free-space optical communications between a transmitter and receiver array, using laser beams. The study takes into account the finite apertures of the arrays and the scattering of a turbulent transmission medium. For the commonly used circular apertures, we connected the two multiplexing approaches using the theory of prolate spheroidal functions. Explicitly, we showed that in regimes with a large number of significant singular values of the transfer matrix (i.e., many modes available for multiplexing), the MIMO approach is the same as the OAM approach for Laguerre-Gauss vortex beams, provided these have a well callibrated initial radius that depends on the wavelength, the distance of propagation and the ratio of the radii of the transmitter and receiver apertures. These communication modes are superior to other vortex beams, for example Bessel-Gauss, which do not take the finite aperture effect into account.

We used the theory of beam propagation in random media to put the phase screen numerical propagation method in a mathematical framework and to clarify the dependence of the phase screen parameters on the Kolmogorov-type model of turbulence. The theory gives theoretical estimates of the communication channel efficiency, which are compared with numerical results obtained with the phase screen method. The results demonstrate the superior performance of the SVD-based multiplexing/demultiplexing approach for communication through a turbulent medium.

A. DETAILS OF THE NUMERICAL CALCULATIONS FOR SVD-BASED MIMO MULTIPLEXING

We consider a transmitter array made of n_T elements with shape (area) $A_{T,t}$, $t = 1, \dots, n_T$, and a receiver array made of n_T elements with shape (area) $A_{R,r}$, $r = 1, \dots, n_R$.

Evaluation of the model transfer matrix. The model transfer matrix $\boldsymbol{\mathcal{T}}$ from element $A_{T,t}$ to $A_{R,r}$ is

$$\mathcal{T}_{r,t} = \int_{A_{R,r}} d\boldsymbol{x} \int_{A_{T,t}} d\boldsymbol{x}' G((\boldsymbol{x}, L), (\boldsymbol{x}', 0)), \tag{46}$$

where G is the paraxial Green's function (10). In the illustration section 2.5, the two arrays are identical with square elements, so that the transfer matrix is complex symmetric.

In practice, the paraxial wave equation is solved in the Fourier domain using the fast Fourier transform (FFT). The model transfer matrix defined in Eq. (46) is computed as follows: 1) we compute the two-dimensional FFT $\widehat{u}_t(\boldsymbol{\kappa}, 0)$ of $u_t(\boldsymbol{x}, 0) = \mathbf{1}_{A_{T,t}}(\boldsymbol{x})$, the indicator function of the source of area $A_{T,t}$; 2) we multiply $\widehat{u}_t(\boldsymbol{\kappa}, 0)$ by $\exp(-i|\boldsymbol{\kappa}|^2 L/(2k))$ to get $\widehat{u}_t(\boldsymbol{\kappa}, L)$; 3) we compute the inverse Fourier transform of $\widehat{u}_t(\boldsymbol{\kappa}, L)$ to get $u_t(\boldsymbol{x}, L)$. This gives $\mathcal{T}_{r,t} = \int_{A_{R,r}} u_t(\boldsymbol{x}, L) d\boldsymbol{x}$.

SVD of the model transfer matrix. We compute the SVD of the model transfer matrix:

$$\boldsymbol{\mathcal{T}} = \mathbf{U}\mathbf{D}\mathbf{V}^{\dagger},$$

where $\mathbf{U}$ and $\mathbf{V}$ are unitary matrices, $\mathbf{D}$ is a diagonal matrix with nonnegative entries, and † stands for conjugate transpose. The columns $\boldsymbol{U}_r$ of $\mathbf{U}$ are the left singular vectors and the columns $\boldsymbol{V}_t$ of $\mathbf{V}$ are the right singular vectors. If the transfer matrix is complex symmetric we can use the symmetric (Takagi) SVD.

SVD-based multiplexing scheme. Let us consider an arbitrary n_T-dimensional vector $\boldsymbol{\beta}_T = (\beta_{T,t})_{t=1}^{n_T}$ to be sent from the transmitter to the receiver. The scheme is:

- *Transmission:* the complex amplitude transmitted by the t-th element $A_{T,t}$ of the transmitter array is $\alpha_{T,t}$ with $\boldsymbol{\alpha}_T = \mathbf{V}\boldsymbol{\beta}_T$. The field sent by the transmitter array is

$$u(\boldsymbol{x}, 0) = \sum_{t=1}^{n_T} \alpha_{T,t} \mathbf{1}_{A_{T,t}}(\boldsymbol{x}).$$

- *Reception:* After propagation through the homogeneous free space, the field in the plane of the receiver array is

$$u(\boldsymbol{x}, L) = \int d\boldsymbol{x}' G((\boldsymbol{x}, L), (\boldsymbol{x}', 0)) u(\boldsymbol{x}', 0).$$

The complex amplitude received by the r-th element $A_{R,r}$ of the receiver array is

$$\alpha_{R,r} = \int_{A_{R,r}} d\boldsymbol{x} u(\boldsymbol{x}, L).$$

That is to say, we get $\boldsymbol{\alpha}_R = \boldsymbol{\mathcal{T}}\boldsymbol{\alpha}_T$.

- *Projection:* for $r = 1, \dots, n_R$, the vector $\boldsymbol{\alpha}_R$ is projected onto the vector $\boldsymbol{U}_r$, so we get

$$\beta_{R,r} = \boldsymbol{U}_r^{\dagger} \boldsymbol{\alpha}_R = (\mathbf{U}^{\dagger} \boldsymbol{\mathcal{T}} \boldsymbol{\alpha}_T)_r = (\mathbf{U}^{\dagger}\mathbf{U}\mathbf{D}\mathbf{V}^{\dagger}\mathbf{V}\boldsymbol{\beta}_T)_r = D_{rr}\beta_{T,r}.$$

This shows that we can extract those entries of $\boldsymbol{\beta}_T$ which correspond to nonzero singular values of the transfer matrix.

ACKNOWLEDGEMENTS

This research is supported in part by AFOSR grants FA9550-18-1-0131 and FA9550-18-1-0217, by ONR grant N00014-17-1-2057 and NSF grant 1616954. The work of the second author was also partially supported by the French ANR under Grant No. ANR-19-CE46-0007 (project ICCI).

DISCLOSURES

The authors declare no conflicts of interest.

REFERENCES

1. G. Gibson, J. Courtial, and M. J. Padgett, "Free-space information transfer using light beams carrying orbital angular momentum," Opt. Express **12**, 5448–5456 (2004).
2. S. M. Barnett, L. Allen, R. P. Cameron, C. R. Gilson, M. J. Padgett, F. C. Speirits, and A. M. Yao, "On the natures of the spin and orbital parts of optical angular momentum," J. Opt. **18**, 064004 (2016).
3. G. J. Gbur, *Singular Optics* (CRC Press, Boca Raton, 2016).
4. Z. Bouchal, "Nondiffracting optical beams: physical properties, experiments, and applications," Czech. J. Phys. **53**, 537–578 (2003).
5. F. Gori, G. Guattari, and C. Padovani, "Bessel-Gauss beams," Opt. Commun. **64**, 491–495 (1987).
6. A. E. Siegman, *Lasers* (University Science Books, Palo Alto, 1986).
7. J. A. Anguita, M. A. Neifeld, and B. . Vasic, "Turbulence-induced channel crosstalk in an orbital angular momentum-multiplexed free-space optical link," Appl. Opt. **47**, 2414–2429 (2008).
8. A. E. Willner, Y. Ren, G. Xie, Y. Yan, L. Li, Z. Zhao, J. Wang, M. Tur, A. F. Molisch, and S. Ashrafi, "Recent advances in high-capacity free-space optical and radio-frequency communications using orbital angular momentum multiplexing," Phil. Trans. R. Soc. A **375**, 20150439 (2017).
9. T. Doster and A. T. Watnik, "Laguerre-Gauss and Bessel-Gauss beams propagation through turbulence: analysis of channel efficiency," Appl. Opt. **55**, 10239–10246 (2016).
10. D. A. B. Miller, "Waves, modes, communications, and optics: a tutorial," Adv. Opt. Photonics **11**, 679–825 (2019).
11. B. Rodenburg, M. P. J. Lavery, M. Malik, M. O'Sullivan, M. Mirhosseini, D. J. Robertson, M. Padgett, and R. W. Boyd, "Influence of atmospheric turbulence on states of light carrying orbital angular momentum," Opt. Lett. **37**, 3735–3737 (2012).
12. M. Chen, K. Dholakia, and M. Mazilu, "Is there an optimal basis to maximise optical information transfer?" Sci. Rep. **6**, 22821 (2016).
13. O. Edfors and A. J. Johansson, "Is orbital angular momentum (OAM) based radio communication an unexploited area?" IEEE Trans. Antennas Propag. **60**, 1126–1131 (2012).
14. A. F. Morabito, L. D. Donato, and T. Isernia, "Orbital angular momentum antennas: Understanding actual possibilities through the aperture antennas theory," IEEE Antenn. Propag. M. **60**, 59–67 (2018).
15. D. Slepian, "Prolate spheroidal wave functions, Fourier analysis and uncertainty - IV: Extensions to many dimensions; generalized prolate spheroidal functions," Bell Syst. Tech. J. **43**, 3009–3057 (1964).
16. R. R. Lederman, "Numerical algorithms for the computation of generalized prolate spheroidal functions," arXiv:1710.02874.
17. J. Shapiro, S. Guha, and B. Erkmen, "Ultimate channel capacity of free-space optical communications," J. Opt. Netw. **4**, 501–516 (2005).
18. B. Rodenburg, "Communicating with transverse modes of light," Ph.D. thesis, University of Rochester (2015).
19. C. Paterson, "Atmospheric turbulence and orbital angular momentum of single photons for optical communication," Phys. Rev. Lett. **94**, 153901 (2005).
20. G. A. Tyler and R. W. Boyd, "Influence of atmospheric turbulence on the propagation of quantum states of light carrying orbital angular momentum," Opt. Lett. **34**, 142–144 (2009).
21. M. J. Padgett and L. Allen, "The Poynting vector in Laguerre-Gaussian laser modes," Opt. Commun. **121**, 36–40 (1995).
22. J. Garnier and K. Sølna, "Coupled paraxial wave equations in random media in the white-noise regime," Ann. Appl. Probab. **19**, 318–346 (2009).
23. K. Itô, "Stochastic integral," Proc. Imp. Acad. Tokyo **20**, 519–524 (1944).